Journal of Physics: Conference Series

PAPER • **OPEN ACCESS**

The dynamical evolution of planetary nebulae

To cite this article: Detlef Schönberner 2016 *J. Phys.: Conf. Ser.* **728** 032001

View the article online for updates and enhancements.

You may also like

- The local dark matter density
J I Read
- The long and winding road from chiral effective Lagrangians to nuclear structure
Ulf-G Meißner
- Modernizing quantum annealing using local searches
Nicholas Chancellor

ECS Membership = Connection

ECS membership connects you to the electrochemical community:

- Facilitate your research and discovery through ECS meetings which convene scientists from around the world;
- Access professional support through your lifetime career:
- Open up mentorship opportunities across the stages of your career;
- Build relationships that nurture partnership, teamwork—and success!

Join ECS! Visit electrochem.org/join

This content was downloaded from IP address 89.245.22.204 on 05/07/2022 at 12:14

Journal of Physics: Conference Series **728** (2016) 032001 doi:10.1088/1742-6596/728/3/032001

The dynamical evolution of planetary nebulae

Detlef Schönberner

Leibniz-Institut für Astrophysik Potsdam (AIP), An der Sternwarte 16, 14482 Potsdam, Germany

E-mail: deschoenberner@aip.de

Abstract. Based on modern 1D-radiation-hydrodynamics simulations of formation and evolution of planetary nebulae, I discuss in detail the basic dynamical processes responsible for the "grand design" of most planetary nebulae, i.e. their double-shell morphology and their typical expansion properties. Special emphasis is given for a proper definition of a nebula's true expansion rate and its relation to spectroscopically measurable Doppler velocities of the expanding material. It is found that the typical nebular expansion is about twice as fast as hitherto assumed, viz. $\simeq 45$ km s^{-1}.

1. The physical system and its modelling

Modern view. The process of formation and evolution of planetary nebulae (PNe) is intimately connected with mass-loss processes along the asymptotic giant branch (AGB) and during the final contraction and heating of the stellar remnant until the white-dwarf stage at the hot side of the Hertzsprung-Russell diagram (HRD) is reached. Thereby, the slow but very dense AGB wind is heated by photo-ionisation due to the intense radiation field of the hot central star which sets up an expanding shock wave and which becomes later compressed from within by the action of the tenuous but very fast central-star wind.

There is, however, no direct interaction of the fast wind with the former AGB matter: The wind is thermalised by a strong shock, and the system's steady attempt to achieve pressure balance between the ionised shell and this shocked wind material on one side, and between the shell and the still undisturbed AGB wind on the other side, is responsible for the formation of what we call a planetary nebula and its evolution with time. In this view, a PN is not only the evidence of matter once ejected from the stellar surface but can instead be described by a thermally driven shock wave through the ambient AGB wind envelope, starting at the inner edge of this envelope and powered by heating due to photo-ionisation. Because of the ever changing boundary conditions, a PN cannot be adequately described by static models or similarity solution for expanding shells.

The concept of expanding shock waves ensures that the system and its morphology remains stable for long times, at least as long as the boundary conditions do not change much. An example of a typical PN structure is rendered in figure 1. One clearly sees a system of two nested shells/shock waves: an inner bright "rim" and a larger but fainter (attached) "shell", both of which consist now of ionised and dynamical "reshaped" former AGB material which expands into the huge, round, even fainter "halo", the just ionised AGB wind. The rim encloses a "cavity", filled with the very hot, shocked wind gas which emit diffuse X-ray radiation (e.g. [2]). The PN proper consist of rim and shell, but note that most of the nebular mass (up to

Content from this work may be used under the terms of the Creative Commons Attribution 3.0 licence. Any further distribution of this work must maintain attribution to the author(s) and the title of the work, journal citation and DOI.
Published under licence by IOP Publishing Ltd

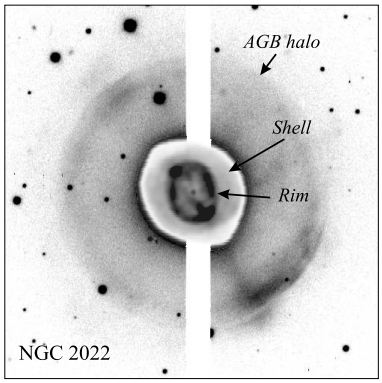

Figure 1. Combination of two [O III] images of the double-shell planetary nebula NGC 2022 with different (logarithmic) intensity scales for inset and main image (see [1] for details). The inset picture shows the PN proper, consisting of rim and shell. The nebula is expanding into the rather large, only slowly expanding round halo, consisting of ionised AGB-wind matter. The central star is about 100 000 K hot and has about 3600 $L_\odot$. The PN has a radius of about 0.2 pc and an estimated kinematic age of about 5000 yr; the halo is much older: $\simeq 40\,000$ yr (cf. [1]).

$\approx 80\,\%$) is contained in the fainter shell! These nebular structures are obviously dynamical stable for expansion timescales of 10 000 years or even longer.

Based on the simple spherical models used in general, we can discuss only the shaping of round nebular structures around single central stars. Though we will show that the physics involved is of basic nature, other shaping mechanism responsible for distortions from sphericity, e.g. rotation, magnetic fields, or binarity, must be studied as well.

Historical review. The modelling of formation and evolution of a planetary nebula by means of hydrodynamics has already a long history. Early attempts ([3, 4]) were, as seen now, not really successful since the boundary conditions were not appropriate: no stellar wind for nebular "support", and expansion of an ad hoc assumed shell into a vacuum. Therefore, the shells of initially constant densities dispersed rather quickly, without showing any similarity to the observed long-lasting double-shell structures as seen in figure 1.

A breakthrough in our understanding of PN formation and evolution was the birth of the famous "interacting stellar winds" (ISW) theory introduced by [5]. These authors were the first who realised that stellar winds which change their properties strongly while the AGB remnant evolves from the tip of the AGB across the HRD are responsible for the formation of PNe: The tenuous but very fast (>1000 km s^{-1}) wind of the hot AGB-remnant (or central star) sweeps-up and engulfs the dense, slow ($\simeq 10$–15 km s^{-1}) relic of the former AGB wind into a well-bounded dense nebular shell which increases permanently its mass and velocity. Follow-up papers presented refinements in terms of time-dependent central-star winds and radiation fields ([6, 7]). With suited chosen wind parameters, reasonable shell expansion velocities ($\simeq 20$ km s^{-1}) could easily be achieved. The weakness of this approach comes from the fact that the hydrodynamics was treated by simple equations that could be solved analytically. The dynamic effects of ionisation could not be treated at all. Also, deep PNe images taken by [8] proved that the double-shell structure of the PN proper as seen in figure 1 is rather the rule, not the exception, whereas the ISW theory is only able to produce *one* expanding shell.

Modern approaches. Relief came from the first numerical 1D radiation-hydrodynamics simulations with realistic initial and time-dependent boundary conditions in the late 80s of the last century ([9, 10]), with some improvements of the wind model introduced later by [11]. The time-dependence refers to stellar post-AGB evolution in terms of stellar and wind parameters and to ionisation/recombination of hydrogen and helium. These simulations showed for the first time that the combined action of ionisation and wind interaction leads automatically to a double shell structure like that seen in figure 1.

In a series of papers, Mellema (e.g. [12, 14, 15]) expanded the previous works in terms of parameter range and better numerics. Mellema ([13]) performed also the first 2D simulations. He computed observable quantities like surface brightness distributions and line profiles/velocity-position diagrams which are necessary for checking the simulations against observations. He emphasised the importance of ionisation as compared to wind interaction and coined the terms

"I-shell" (I = ionisation) for the shell and "W-shell" (W = wind) for the rim in order to account for the different physics at work.

A more comprehensive study was performed by Villaver *et al* [16, 17]. These authors used the evolutionary AGB and post-AGB models of Vassiliadis and Wood ([18, 19]) including their (assumed) mass-loss rates and computed in a consistent way the hydrodynamical evolution of the stellar envelopes together with the central stellar object along the AGB and post-AGB. The predictive power of this study is, however, limited for the following reasons: (1) ionisation is treated by Strömgren spheres with a constant temperature of 10^4 K, and (2) no observables like intensity distributions or emission-line profiles have been computed.

The most sophisticated simulations so far are those presented by [20] and later by [22]. The code (NEBEL) is fully time-dependent, i.e. the actual ionisation/recombination and heating/cooling is computed at each time step, based on the prevailing ensemble of existing species, the physical state of the plasma, and the radiation field. Nine relevant elements up to argon and their ionisation stages are considered (fore more details, see [21] and the references therein). The NEBEL code includes also heat conduction by electrons which is important for a realistic description of the temperature and density profiles inside the bubble of shocked wind gas. Additional IDL-routines allow the (a posteriori) computation of a number of observable entities like emission-line strengths and profiles, intensity distributions, and X-ray emission from the hot bubble. In a series of papers, issues like circumstellar environment and expansion ([23]), internal kinematics and expansion ([24]), individual luminosity functions ([25]), diffuse X-ray emission ([26]), the extremely metal-poor PN G135.9+55.9 ([27]), PNe in distant stellar systems ([28]), and true expansion rates and visibilities of PNe ([29]) have been addressed.

Very recently, Toála and Arthur ([31]) computed spherical models in a similar way as in

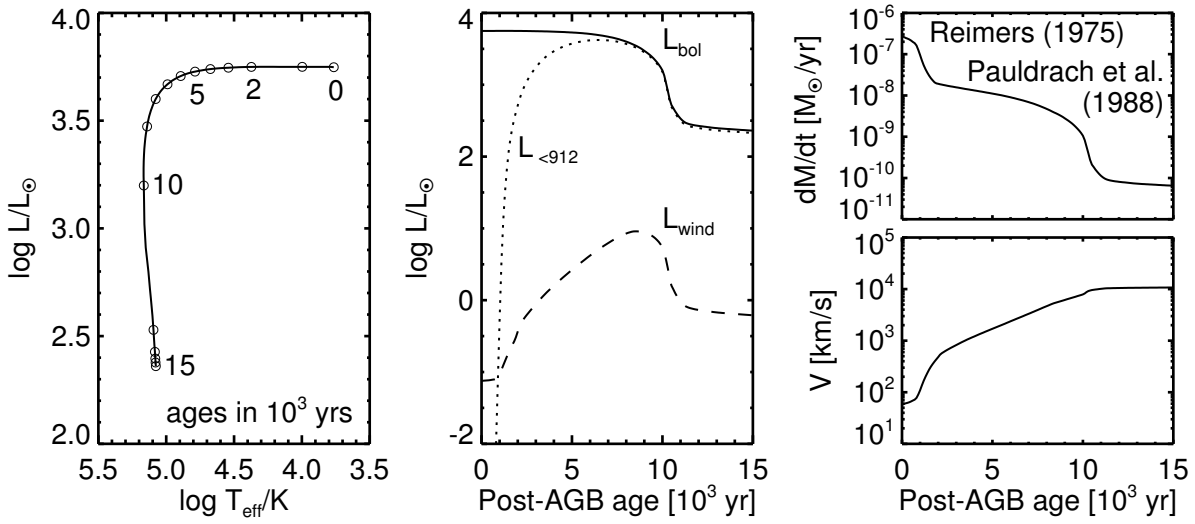

Figure 2. Example of stellar and wind properties used in our radiation-hydrodynamical simulations for the inner boundary conditions. *Left panel*: evolutionary path for a 0.595 $M_\odot$ post-AGB model with ages indicated; *middle panel*: the corresponding time evolution of the bolometric, $L_{\rm bol}$ (solid), Lyman continuum, $L_{<912}$ (dotted), and mechanical (wind) luminosity, $L_{\rm wind} = \dot{M}\,V^2/2$ (dashed), all in solar units. *Right panels*: mass-loss rate $\dot{M}$ (*top*) and wind velocity V (*bottom*). The end of the strong, dense AGB wind sets the zero point of the post-AGB evolution and the beginning of the much weaker post-AGB wind, modelled first by the prescription of Reimers ([32]). Later, for $T_{\rm eff} \geq 25\,000$ K, or post-AGB ages $\geq 2{\times}10^3$ years, the theory of radiation-driven winds as formulated by Pauldrach *et al* ([35]) is used for the rest of the evolution.

[16] but allowed for 2D effects like, e.g., Rayleigh-Taylor instabilities and mixing between "cool" nebular and "hot" shocked wind gas. To date it is too early to judge the quality of these models because detailed comparisons between the models and real objects are still pending.

Example of hydrodynamical PN modelling. In the following, I will thus refer mainly to results presented and discussed in [30], where an extensive comparison between 1D radiation-hydrodynamical PN models and the observations can be found. Thereby it is implicitly assumed that spherical models are able to give, at least on the average, a reasonable description of real objects, provided the distortion from sphericity of the latter is not too big.

The typical inner boundary conditions as they are given by the properties of an evolving central star are illustrated in figure 2. By comparing the wind power with that of the ionising radiation, one notices that the former increases only slowly and reaches a maximum value close before maximum stellar temperature is reached. The reason is the evolution of the wind velocity which is coupled to the stellar escape velocity and more than compensates for the slowly decreasing mass-loss rate until the white-dwarf stage with nearly constant stellar radius is reached (cf. right panels of figure 2).

The low wind power during the early PN evolution implies that its influence for shaping young objects is most likely rather small. This statement does not change even if one considers the uncertainty of the "early" post-AGB mass-loss rate which is assumed here to be of Reimers' type ([32]): The wind velocity is just too low. The mass-loss uncertainty translates, however, directly into the transition timescale of an AGB remnant from the tip of the AGB to, say, a position in the HR diagram with an effective temperature of about 25 000 K (cf. [33, 34]). We used in the simulations the older post-AGB mass-loss rates and wind velocities of Pauldrach *et al* ([35]) in order to be consistent with the evolutionary models of Blöcker ([34]). The more recent post-AGB mass-loss rates and wind velocities derived by Pauldrach *et al* ([36]) are somewhat different from the ones used here, but not by so much that existing hydrodynamical models are put into question, especially if one considers all the other uncertainties.

In order to cover a reasonable number of possible combinations between central star and initial envelope, a grid of PN simulations have been used in [30], encompassing central-star masses from $\simeq 0.57$ to $\simeq 0.70$ $M_\odot$ which are coupled to either envelopes with initial density profiles based on hydrodynamics of dusty envelopes on the AGB ([37]) or initial envelopes with simple radial power-law density distributions.

Figure 3 renders a typical middle-aged and fully ionised nebular structure taken from a simulation along the model track shown in figure 2 at a position in the HRD given in the figure caption. We see, next to the ionisation-generated shell which makes up for most of the nebula, also an already well-developed rim, and both are bounded by respective shocks whose radial positions are marked in the figure as well. The shell is somewhat diluted because it has already expanded into the former AGB wind with a rather steep density gradient, while the rim is of much higher density because of the bubble's comparatively high pressure, i.e. the rim's shock is catching up with the shell, thereby compressing and engulfing the inner shell matter. Consequently, both the rim and the shell show a very distinct behaviour in their radial density and velocity profiles, thus also their contribution to the intensity distributions and line profiles are distinct. Note especially the rather faint signatures of the shell in [O III] in both the brightnesses and line profiles, although the shell contains most of the nebular mass, i.e. 85 % of the $0.47\,M_\odot$ of ionised matter contained in the PN model shown in the left panel of figure 3. Note especially the rather low flow velocities within the rim, ≈ 12 km s^{-1}, as compared to the post-shock velocity of the shell, 30 km s^{-1}.

We emphasise here two facts: (1) Shell and rim are two distinct entities of a PN that are created by two different physical mechanisms, viz. ionisation and winds interaction, and (2) both have hence different expansion properties. Furthermore, the overall velocity field does not obey a simple $v(r) \propto r$ law, as generally assumed in spatio-kinematical modelling.

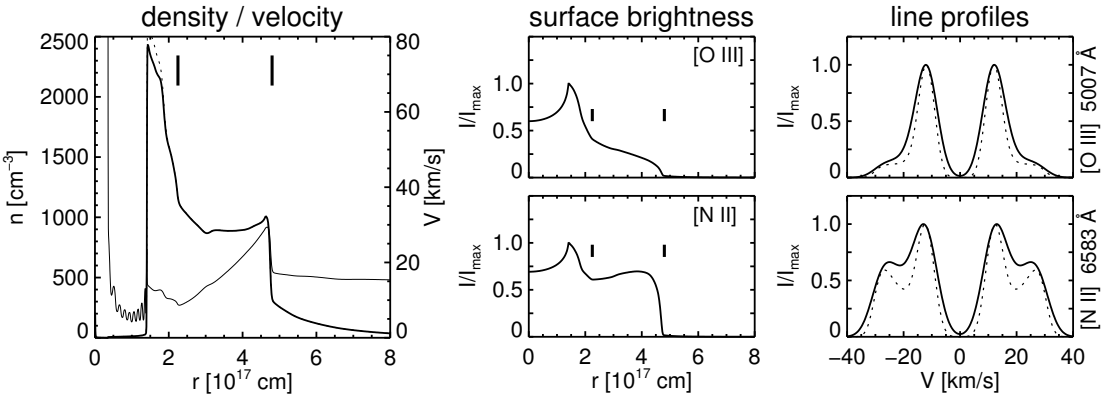

Figure 3. Snapshot of a typical middle-aged nebular model from a 1D-radiation-hydrodynamics simulation around a 0.595 $M_\odot$ central star whose properties are shown in figure 2. The stellar parameters are: post-AGB age $t = 6106$ yr, $T_{\rm eff} = 80\,177$ K, and $L = 5.057{\times}10^3$ $L_\odot$. *Left panel*: heavy particle density (thick), electron density (dotted), and gas velocity (thin); *middle panels*: (normalised) surface brightnesses in [O III] λ5007 Å and [N II] λ6583 Å; *right panels*: the corresponding normalised line profiles computed for the central line-of-sight with infinite spectral resolution (dotted) and broadened with a Gaussian of 6 km s^{-1} FWHM (solid), both with a circular aperture of $1{\times}10^{16}$ cm. The line-profile peaks are the signature of the rim, while the fainter "shoulders" belong to the shell. The thick vertical marks (*left and middle*) indicate the positions of the leading shocks of the rim and shell, respectively. The nebular mass enclosed by the rim's shock is $M_{\rm rim} = 0.07$ $M_\odot$, that enclosed by the shell's leading shock is $M_{\rm shell} = 0.47$ $M_\odot$ (= total nebular mass). The shell's shock defines the outer edge of the PN.

Before continuing, we must emphasise that all the hydrodynamical simulations discussed here neglect magnetic fields. Whether they are responsible for shaping non-spherical PNe is still an open question. On the existence of magnetic fields in PNe, see also the recent work of Steffen *et al* ([38]).

Additionally, one should note also that both the stellar post-AGB models and the mass-loss modelling refer to objects which have normal stellar surface composition and which burn hydrogen while evolving across the HR diagram. Nebulae with hydrogen-deficient central stars are *not* considered because (1) the latter have much stronger winds with corresponding stronger dynamical impact on the nebula and (2) their formation and evolution is yet totally unknown.

2. Expansion properties of PNe

Although the typical "expansion velocity" of PNe is a quantity of utmost importance for a number of contexts, it is only poorly defined and cannot be specified without knowledge of the density structure and internal velocity field of the object in question. It is therefore important to use hydrodynamical models to get more insight into the expansion properties of PNe.

Guided by the model in figure 3, we can state that the velocity of the shell's leading shock ($\dot{R}_{\rm PN}$ at $r = R_{\rm PN} = 4.7{\times}10^{17}$ cm), whose position defines also the outer edge of the PN, is the *true* expansion velocity. Unfortunately, the propagation speed of this shock *cannot* be measured spectroscopically since it is a "pattern", not "matter" expansion! Several different definitions of the expansion velocity of PNe are in use, and their correspondence to the true expansion velocity $\dot{R}_{\rm PN}$ is a priori not clear at all.

1. Half-width of spatially/spectroscopically unresolved lines. Very uncertain relation to $\dot{R}_{\rm PN}$, and the latter can be up to three times higher (cf. figure 39 in [28]), depending on the phase of evolution. This velocity value should *not* be used at all since it is strongly biased towards the object's dense, low velocity structures.

2. Peak separation of resolved lines. A very frequently used method, but provides only the bulk velocity of the rim, $V_{\rm rim}$, which is usually well below $\dot{R}_{\rm PN}$ (see below). The canonical values of the PN expansion velocity used in the literature, 20–25 km s^{-1}, are mainly based on this method.

3. Post-shock velocity. A method introduced by Corradi *et al* ([39]): The (outer) inflection points of the line-profile shoulders as seen in figure 3 (right panels) are a good measure of the shell's shock post-shock gas velocity. This post-shock velocity is closely related to the shock propagation speed itself: $\dot{R}_{\rm PN} = V_{\rm post} \times F$, with $F > 1$. The value of F depends on the shock properties, and by means of PN models from different simulations, Schönberner *et al* ([30], figure 6 therein) found that a very reasonable value is $F = 1.25 \pm 0.05$ (optically-thin models only). Mellema ([40]) found a similar value, $F = 1.2$, by employing the jump conditions together with reasonable assumptions for the shell's shock properties.

The velocities measured by methods 1 and 2 may depend on the ion used and have unknown relations to the true expansion given by $\dot{R}_{\rm PN}$. Only method 3 leads to a physically sound velocity value, rather independently of the used species and close to the real expansion rate. Of course, the term "expansion velocity" as used here is only applicable for objects where we can be sure about the existence of a more or less regularily expanding shell.

In order to get more insight into the internal kinematics and expansion properties of PNe, Schönberner *et al* ([30]) analysed spatially resolved emission-line profiles of about 20 elliptical PNe. The bulk velocity of the rim, $V_{\rm rim}$, was measured from the line-peak separations, and the post-shock velocity, $V_{\rm post}$, from the line shoulders' inflection points, as discussed above. The results are rendered in figure 4, where the stellar effective temperature is used as proxy for the pace of evolution. One can conclude the following:

- The shell's edge expands considerably faster than the rim, but both accelerate during the evolution with $T_{\rm eff}$ (or time), albeit in a different way. The post-shock velocity of the shell increases with $\log T_{\rm eff}$ from about 15–30 km s^{-1} up to about 35–45 km s^{-1} at $\log T_{\rm eff} \geq 4.8$. In contrast, the rim is stalling at rather low velocities ($\simeq$5–10 km s^{-1}) for quite a while until it finally accelerates up to about 25–30 km s^{-1}.
- The initial shell expansion starts with post-shock flow speeds *exceeding* those at the tip of the AGB where outflow velocities of $\approx$10–15 km s^{-1} are typical. The rim gas, however, has initially velocities which are close or even well *below* the tip-AGB outflow velocities. Important is that for these younger PNe the post-shock velocity of the shell exceeds the rim expansion by factors up to five to six ($\sim$6 km s^{-1} vs. $\sim$34 km s^{-1} for NGC 6629)! In more advanced stages, $V_{\rm post}$ (and $\dot{R}_{\rm PN}$) still exceeds $V_{\rm rim}$ by factors well above unity.

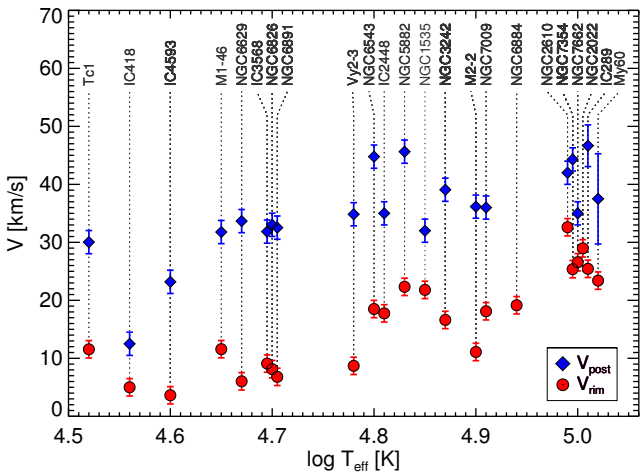

Figure 4. Shell post-shock velocities, $V_{\rm post}$ (blue diamonds), and rim bulk velocities, $V_{\rm rim}$ (half of line peak separation, red dots), of the objects investigated vs. $T_{\rm eff}$ of the respective central stars. There are generally two velocity entries for each object, except for those for which the post-shock velocity could not be measured (NGC 2022 and NGC 6894). Velocities are either from [N II] or [O III], or averaged if information from both ions is available. Vertical dotted lines connect the two velocities with the object's name. Some object entries are slightly shifted in temperature as to avoid overlapping.

These measurements fully confirm the basic predictions of the radiation-hydrodynamic simulations discussed above and illustrated in figure 3: It is the ionisation that sets up the expansion of a PN shell, not the stellar wind. Only in the more advanced stages of evolution plays the winds interaction a larger role. The high expansion speed of the shell's shock is obviously due to the steep density gradient of the upstream (= halo) matter, as predicted by analytical similarity solutions (cf. [41]) and confirmed by dedicated hydrodynamical simulations ([30]). In terms of power-law density distributions $\rho \propto r^{-\alpha}$, the observed post-shock gas velocities correspond to $\alpha \simeq 2.8$–3.4. Direct measurements of the halo density distributions from the observed intensity distributions give virtually the same answer (cf. [42, 30]).

We emphasise that the shock speed does *not* depend on the upstream density itself. Furthermore, the general steep density gradient means that the mass-loss rate increases immediately before the object departs from the tip of the AGB, thereby quenching the high mass-loss rate. Using the correction factor F to convert the observed post shock velocities into the respective shock speeds, one gets a reasonable value of the true PN expansion velocity, at least for the sample studied, of $\langle \dot{R}_{\rm PN} \rangle \simeq 45$ km s^{-1}, as compared to $\langle V_{\rm rim} \rangle \simeq 20$ km s^{-1}. A more comprehensive study concerning the true expansion rate of PNe and its relevance for the visibility time can be found in [29].

The ultimate test of the hydrodynamical models is provided by objects with lower metallicities. The weaker winds of metal-poor central stars lead to more slowly expanding rims, or no rims at all for the extreme metal-poor cases (cf. [28] for the details). In contrast, the high electron temperatures let the shell expand faster (cf. [41]), making the shell more diluted and fainter. Schönberner *et al* ([30]) succeeded in measuring $V_{\rm rim}$ *and* $V_{\rm post}$ for 4 metal-poor objects, and the results confirm the models (see figure 5): there is a tendency of $V_{\rm post}$ for being higher and for $V_{\rm rim}$ being lower than is typical for Milky Way disk objects at similar evolutionary stages, fully consistent with the predictions of the dynamical nebular models as presented here.

3. Summary

Modern radiation-hydrodynamics simulations, even in the 1D approximation, yield new insights into the formation and evolution of round/elliptical planetary nebulae:

- The often observed double-shell morphology is a natural consequence of ionisation and winds interaction, where shell and rim are driven by different physical mechanism: A shock wave is set up either by heating of circumstellar gas due to ionisation (shell) or by expansion of the hot, shocked wind gas (rim).

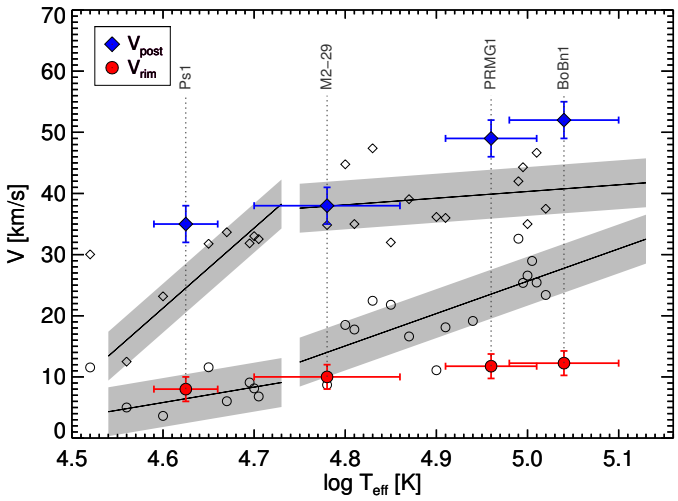

Figure 5. Same as figure 4, but with the positions of 4 metal-poor PNe, with horizontal bars indicating the range of temperature determinations. The general run of the velocities with effective temperatures for the PNe in the Milky Way disk are shown in a schematic way as well. The objects from figure 4 are underlain as small open diamonds and circles.

- The true mean expansion velocity of PNe isusually higher than hitherto assumed, $\simeq 45$ km s^{-1}, given by the expansion of the shell's leading shock which is exclusively ruled by electron temperature and upstream density gradient. The rim's expansion is much lower and does in general not exceed $\simeq 30$ km s^{-1}.
- The high shell expansion of PNe is caused by a rather steep halo density gradient ($\alpha \simeq 3$), which in turn means that the mass-loss rate during the past final AGB stage must have increased steadily.
- The shells of metal-poor PNe expand faster than their disk counterparts because of their high electron temperatures. On the other hand, their central cavity is smaller because of the weak stellar wind.

References

[1] Corradi R L M, Schönberner D, Steffen M and Perinotto M 2003 *Mon. Not. R. Astron. Soc.* **340** 417
[2] Kastner J H *et al* 2012 *Astron. J.* **144** 58
[3] Mathews W G 1966 *Astrophys. J.* **144** 206
[4] Ferch R L and Salpeter E E 1975 *Astrophys. J.* **202** 195
[5] Kwok S, Purton C R and Fitzgerald P M 1978 *Astrophys. J.* **219** L125
[6] Kwok S 1982 *Astrophys. J.* **258** 280
[7] Volk K and Kwok S 1985 *Astron. Astrophys.* **153** 79
[8] Chu Y-H, Jacoby G H and Arendt R 1987 *Astrophys. J. Suppl. Series* **64** 529
[9] Schmidt-Voigt M and Köppen J 1987 *Astron. Astrophys.* **174** 211
[10] Schmidt-Voigt M and Köppen J 1987 *Astron. Astrophys.* **174** 223
[11] Marten H and Schönberner D 1991 *Astron. Astrophys.* **248** 590
[12] Mellema G 1994 *Astron. Astrophys.* **290** 915
[13] Mellema G 1995 *Mon. Not. R. Astron. Soc.* **277** 173
[14] Mellema G 1997 *Astron. Astrophys.* **321** L29
[15] Mellema G and Frank A 1995 *Mon. Not. R. Astron. Soc.* **273** 401
[16] Villaver E, García-Segura G and Manchado A 2002 *Astrophys. J.* **571** 880
[17] Villaver E, Manchado A and García-Segura G 2002 *Astrophys. J.* 581 1204
[18] Vassiliadis E and Wood P 1993 *Astrophys. J.* **413** 64
[19] Vassiliadis E and Wood P 1993 *Astrophys. J. Suppl. Series* **92** 125
[20] Schönberner D, Steffen M, Stahlberg J, Kifonidis K and Blöcker T 1997 *Workshop Stellar Ecology: Advances in Stellar Evolution* ed R T Wood and A Renzini p 146
[21] Perinotto M, Kifonidis K, Schönberner D and Marten H 1998 *Astron. Astrophys.* **332** 1044
[22] Perinotto M, Schönberner D, Steffen M and Calonaci C 2004 *Astron. Astrophys.* **414** 993
[23] Schönberner D, Jacob R, Steffen M, Perinotto R L M and Acker A 2005 *Astron. Astrophys.* **431** 963
[24] Schönberner D, Jacob R and Steffen M 2005 *Astron. Astrophys.* **441** 573
[25] Schönberner D, Jacob R, Steffen M and Sandin C 2007 *Astron. Astrophys.* **473** 467
[26] Schönberner D, Steffen M and Warmuth A 2008 *Astron. Astrophys.* **489** 173
[27] Sandin C, Jacob R, Schönberner D, Steffen M and Roth M M 2010 *Astron. Astrophys.* **512** A18
[28] Schönberner D, Jacob R, Sandin C and Steffen M 2010 *Astron. Astrophys.* **523** A86
[29] Jacob R, Schönberner D and Steffen M 2013 *Astron. Astrophys.* **558** A78
[30] Schönberner D, Jacob R, Lehmann H, Hildebrandt G, Steffen M, Zwanzig A, Sandin C and Corradi R L M 2014 *Astronomische Nachrichten* **335** 378
[31] Toalá J A and Arthur S J 2014 *Mon. Not. R. Astron. Soc.* **443** 3486
[32] Reimers D 1975 *Problems in Stellar Atmospheres and Envelopes* ed B Baschek *et al* (Springer, Berlin) p 229
[33] Schönberner D and Blöcker T 1993 *Luminous High Latitude Stars* ed D Sasselov *ASP Conf. Series* **45** p 337
[34] Blöcker T 1995 *Astron. Astrophys.* **299** 755
[35] Pauldrach A W A, Puls J, Kudritzki R-P, Méndez R H and Heap S 1988 *Astron. Astrophys.* **207** 123
[36] Pauldrach A W A, Hoffmann T L and Méndez R H 2004 *Astron. Astrophys.* **419** 1111
[37] Steffen M, Szczerba R and Schönberner D 1998 *Astron. Astrophys.* **337** 149
[38] Steffen M, Hubrig S, Todt H, Schöller M, Hamann W-R, Sandin C and Schönberner D 2015 *Astron. Astrophys.* **570** A88
[39] Corradi R L M, Steffen M, Schönberner D and Jacob R 2007 *Astron. Astrophys.* **474** 529
[40] Mellema G 2004 *Astron. Astrophys.* **416** 623
[41] Chevalier R A 1997 *Astrophys. J.* **488** 263
[42] Plait P and Soker N 1990 *Astron. J.* **99** 1883